

Analysis of gravitational waves from binary neutron star merger by Hilbert-Huang transform

Masato Kaneyama,¹ Ken-ichi Oohara,² Hirotaka Takahashi,^{3,4} Yuichiro Sekiguchi,⁵
Hideyuki Tagoshi,¹ and Masaru Shibata⁶

¹*Department of Physics, Graduate School of Science, Osaka City University, Osaka 558-8585, Japan*

²*Graduate School of Science and Technology, Niigata University, Niigata 950-2181, Japan*

³*Department of Information and Management Systems Engineering, Nagaoka University of Technology, Nagaoka, Niigata 940-2188, Japan*

⁴*Earthquake Research Institute, The University of Tokyo, Bunkyo-Ku, Tokyo 113-0032, Japan*

⁵*Department of Physics, Toho University, Funabashi, Chiba 274-8510, Japan*

⁶*Center for Gravitational Physics, Yukawa Institute for Theoretical Physics, Kyoto University, Kyoto 606-8502, Japan*

(Received 31 January 2016; published 17 June 2016)

Using the Hilbert-Huang transform (HHT), we analyze gravitational waves from late inspiral, merger, and post-merger phases of binary neutron stars coalescence, computed by a general relativistic numerical simulation. The HHT analysis has been developed as a method for time series analysis of nonlinear and nonstationary data, and it enables us to perform a high resolution time frequency analysis of signals with strong frequency modulation by evaluating the instantaneous variation of amplitude and frequency of data. We find that we can clearly observe the time evolution of the instantaneous frequency of the post-merger waveforms. It is found that temporal variation of frequency of post-merger waveforms can be evaluated within 5% error if BNS coalescences occur within 10 Mpc. This accuracy allows us to constrain the equation of state of neutron stars and to evaluate the radius of a fiducial neutron star of $1.8M_{\odot}$ with a few hundred meters accuracy.

DOI: [10.1103/PhysRevD.93.123010](https://doi.org/10.1103/PhysRevD.93.123010)

I. INTRODUCTION

Advanced LIGO detectors [1] recently observed the first gravitational-wave (GW) signal from merging black holes with high statistical significance [2].

Gravitational waves produced by the coalescence of binary neutron stars (BNSs) are also a promising source for ground-based GW detectors, Advanced LIGO, Advanced Virgo [3], and KAGRA [4]. When GWs from BNSs are observed, we can constrain the equation of state (EOS) of the neutron stars (NSs) and can examine the hypothesis of the central engine of short γ -ray bursts. The detection rate of such events for the ground-based GW detectors is estimated to be 4–400 yr⁻¹ by theoretical and statistical studies [5].

The EOS of high-density nuclear matter for NSs is still poorly known. Under assumptions that a NS is in cold, spherically symmetric, general relativistic, hydrostatic equilibrium, there is one-to-one correspondence between the EOS and mass-radius relation of NSs [6]. Therefore, the EOS will be constrained if the mass and radius of NSs are evaluated through the observation of GWs from coalescences of BNS.

Many hypothetical EOSs have been proposed from the theoretical study in nuclear physics. Each EOS is characterized by the maximum mass of neutron stars. NSs of high mass such as $1.97 \pm 0.04M_{\odot}$ [7] and $2.01 \pm 0.04M_{\odot}$ [8] have been discovered through electromagnetic observations.

The existence of these NSs suggest that the maximum mass of NSs must predict greater than $2M_{\odot}$.

Recently, the gravitational waveforms from the coalescences of BNS and dynamics of post-merger phase have been explored in detail by general relativistic numerical simulations (e.g., [9–14]). These gravitational waveforms reflect the mass and the EOS of NSs as well as the dynamics of the BNS merger. A black hole is promptly formed after the coalescences for soft EOSs or for high-mass BNS, while a massive NS (MNS) is formed after the coalescences for stiff EOSs or for low-mass BNS. We note that the mass of MNS can be heavier than the maximum mass of spherical NSs, since MNSs formed after the coalescences are supported by thermal pressure and the centrifugal force resulting from rapid and differential rotation.

Previous studies [11–13] have suggested the possible presence of a relation between the radius of a fiducial NS and a peak frequency of dominant quadrupolar mode in the Fourier spectrum of GWs from MNSs. If we can determine the peak frequency, the radii of a fiducial NS will be constrained, leading to a strong constraint of the EOS of NSs. This information allows us to constrain the EOS of NSs. In Ref. [15], after the detection of GW from MNSs by the coherent WaveBurst, the peak frequencies are characterized by reconstructed post-merger signal. Clark *et al.* [16] attempted a construction of templates of post-merger signals by using principle component analysis. Both studies

show that the EOSs of NSs are strongly constrained by observing GWs from MNS.

In this paper, we explore another possibility to obtain information on EOS from the time evolution of the instantaneous frequency of GW from MNS by using the Hilbert-Huang transform (HHT). The HHT, which consists of an empirical mode decomposition followed by the Hilbert spectral analysis, has been developed by Huang *et al.* [17–19]. Compared with the Fourier decomposition and wavelet decomposition, the empirical mode decomposition approach has an advantage for analyzing the nonstationary and nonlinear data since it decomposes the signal into intrinsic mode functions based on the time scale of the signal itself with adaptive nature. The HHT is not limited by time-frequency uncertainty, and thus, it provides a high resolution time-frequency analysis.

The HHT is a powerful tool to extract the information from the gravitational waveforms. Applications of the HHT to the data analysis of GWs, mainly from burst sources including supernovae and coalescence of supermassive black holes, have already been proposed in Refs. [20–25]. It could also be a powerful tool for analyzing GWs from the BNS coalescences, in particular, for the merger and post-merger phases. In this paper, we describe a method for analyzing GWs from late inspiral, merger, and post-merger phases of BNSs using the HHT, after the detection of post-merger signals. We use gravitational wave signals from late inspiral, merger, and post-merger phases of BNS coalescences computed with numerical relativity simulations.

We consider two kinds of EOS. One is a finite-temperature EOS that includes contributions of Λ hyperons (Hyp-EOS). The other is a purely nucleonic EOS (Shen-EOS).

The numerical simulation data show that the instantaneous frequency of the post-merger signals from MNS increase with time in the case of Hyp-EOS. But no such evolution is found for Shen-EOS.

We inject those signals into the simulated noise of Advanced LIGO and analyze the data with HHT. We find that, when the source is located at 10 Mpc, we can clearly identify the frequency evolution of the post-merger signals on the time-frequency map which frequency evolution agrees with the injected signals. We confirm that we can distinguish the difference of the frequency evolution between two EOS models.

The paper is organized as follows. In Sec. II, we briefly review the Hilbert-Huang transform. In Sec. III, we briefly describe the numerical waveforms that we employ in this paper. In Sec. IV, the results of the HHT analysis are shown and the implication of the results is discussed. In Sec. V, we discuss the accuracy of derived instantaneous frequency of GWs from MNS. Section VI is devoted to a summary.

II. THE HILBERT-HUANG TRANSFORM

In this section, we briefly review the HHT. The HHT analysis consists of two parts. The first one is the empirical mode decomposition (EMD), in which the time-series data are decomposed into intrinsic mode functions (IMFs). This is just a preconditioning for the next step. In the second part of the HHT, the Hilbert transform is applied to each IMF, and we obtain an analytic complex representation of each IMF. From this, we derive the instantaneous frequency (IF) and the instantaneous amplitude (IA) of each IMF. This part is called the Hilbert spectrum analysis (HSA). The IF and IA provide a time-frequency representation of data that is well suited for resolving nonlinear and transient features of the original data.

We assume that the input $s(t)$ is given by sampling a continuous signal at discrete time series, $t_j = j\Delta t$ for $j = 0, 1, \dots, N - 1$, where N is the number of data points and Δt is the sampling interval.

A. Empirical Mode Decomposition and Ensemble empirical mode decomposition

1. Empirical mode decomposition

For any time-series data, it is known that the Hilbert transform of the data does not always yield physically meaningful results. Huang *et al.* [18] showed that the IA and IF have physically meaningful results if the time-series data satisfy the following conditions (hereinafter referred to as the IMF condition):

- (A) For all data sets, the number of extrema and the number of zero crossings have to either be identical or differ at most by one.
- (B) At any data point, the mean values of the upper and the lower envelopes defined by using the local maxima and minima, respectively, have to be zero.

These empirical conditions indicate that the data have a vertical symmetry around zero point. However, the observational data $s(t)$ do not generally satisfy these conditions. Thus, the observational data $s(t)$ should be decomposed by using the EMD. When using the EMD, we implicitly assume that, at any given time, the data may have many coexisting oscillatory modes of significantly different frequencies, one superimposed on the other. For each of these modes, we define an IMF that satisfies the IMF condition. With the definition of the IMF, we can thus decompose any data through the EMD, which, in a sense, is a sifting process using a series of high-pass filters. The outline of this algorithm is summarized as follows, and Fig. 1 shows a schematic example of this procedure.

The above procedures are summarized as follows. In the beginning, we set $g(t) = s_1(t) = s(t)$, using the original data. Then the EMD procedure is performed identifying all the local extrema (Fig. 1(a)). The local maxima and minima

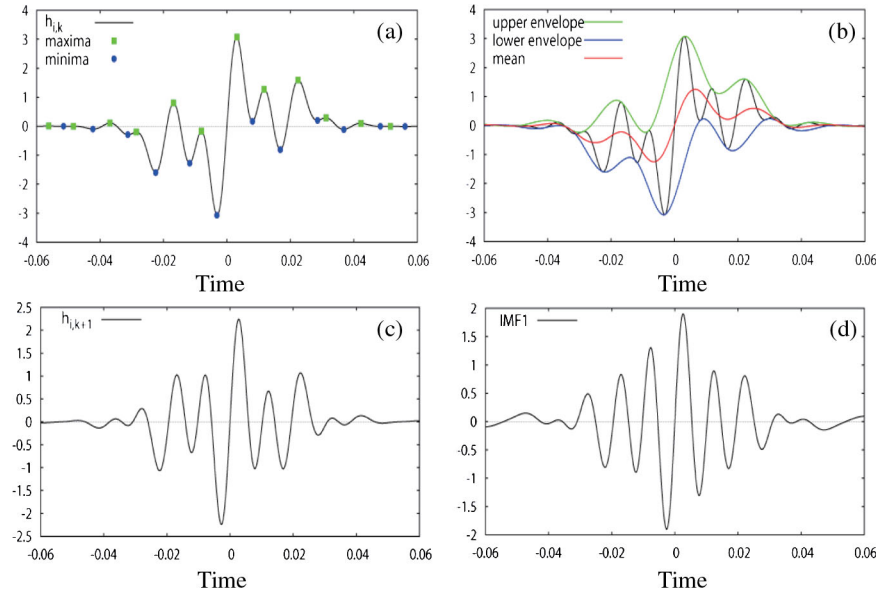


FIG. 1. Outline of EMD sifting algorithm and schematic example. Note that the magnitude of the vertical axis gradually decreases in each step. (a) Local extrema of time series. (b) Upper and lower envelopes formed by connecting extrema and their mean. (c) Subtraction of mean from time series. (d) IMF1 obtained after several iterations.

are connected by cubic splines to form the upper envelope $U(t)$ and the lower envelope $L(t)$, respectively (Fig. 1(b)). All data are usually encompassed between them. Let their mean $m(t) = (U(t) + L(t))/2$ and update $g(t)$ by subtracting it from $g(t)$ to obtain the first proto-mode; $g(t) = g(t) - m(t)$ (Fig. 1(c)). The mean $m(t)$ contains the DC offset and components in a low frequency band of the signal, and therefore, $g(t)$ is expected to satisfy the IMF condition. However, that is usually not the case, but iteration of the above procedure is necessary if $g(t)$ still contains two or more oscillatory components. Finally, $g(t)$ becomes the IMF1, $c_1(t) = g(t)$, if the IMF condition is satisfied approximately after several iterations (Fig. 1(d)).

In practice, these conditions are not satisfied precisely. Thus, we have to define an approximate criterion for stopping the interaction procedure. This is controlled by a stoppage criterion. Several different types of stoppage criteria have been adopted. In this paper, we use a criterion determined by using the Cauchy type of convergence test, which was used in [18]

$$\frac{\sum_{j=0}^{N-1} |m(t_j)|^2}{\sum_{j=0}^{N-1} |g(t_j)|^2} < \epsilon, \quad (1)$$

with a predetermined value ϵ .

The first IMF1 $c_1(t)$ should contain the finest scale or the shortest-period oscillation in the signal. It is subtracted from the original data to obtain the residual $s_2(t) = s_1(t) - c_1(t)$, which contains the longer-period oscillations. It is then treated as a new data source and subject to the

same process of EMD as described above to obtain the IMF of the next lowest frequency.

The procedure is iteratively applied to all subsequent $s_i(t)$. The decomposition process finally stops when the residual, $s_{n+1}(t)$, becomes monotonic or has only one extremum, from which no more IMF can be extracted. Then, the original data are decomposed into n IMFs and a residue, $r(t) = s_{n+1}(t)$; $s(t) = \sum_{i=1}^n c_i(t) + r(t)$. The residue $r(t)$ can be either the adaptive local median or trend. In practice, numerical errors occasionally prevent the residual $s_{n+1}(t)$ from being monotonic, and thus, the decomposition process is ceased if the residual becomes much smaller than previous IMFs.

2. Ensemble empirical mode decomposition

In the original form of EMD, however, mode mixing often occurs when either a single IMF consists of signals of widely disparate scales, or when signals of a similar scale reside in different IMF components. To mitigate this effect, Wu and Huang [26] proposed ensemble EMD (EEMD), which defines the true IMF components as the mean of an ensemble of trials, each consisting of the signal plus a white (Gaussian) noise of finite standard deviation (finite amplitude).

The EEMD algorithm is composed of the following steps:

- (i) Add a white (Gaussian) noise with the standard deviation σ_e to the original data $s(t)$.
- (ii) Decompose the data with the white noise into IMFs.

- (iii) Repeat steps (i) and (ii) several times but with a different white Gaussian noise series at each time.
- (iv) Obtain the ensemble means for the series of the obtained IMFs of the decompositions. The number of trials, N_e , has to be larger than 100.

Algorithm Empirical Mode Decomposition (EMD)

procedure EMD ($s(t)$)

```

 $s_1(t) \leftarrow s(t)$ 
 $i \leftarrow 1$ 
while  $s_i(t)$  includes oscillatory modes do
    ▷ See Note 1 below.
     $g(t) \leftarrow s_i(t)$ 
    repeat
         $g_{\max}[j] \leftarrow$  local maxima of  $g(t)$  (Fig. 1(a))
         $g_{\min}[j] \leftarrow$  local minima of  $g(t)$ 
         $U(t) \leftarrow$  the upper envelope joining  $g_{\max}[j]$ 
         $L(t) \leftarrow$  the lower envelope joining  $g_{\min}[j]$ 
        using cubic splines, respectively
         $m(t) \leftarrow (U(t) + L(t))/2$  (Fig. 1(b))
         $g(t) \leftarrow g(t) - m(t)$  (Fig. 1(c))
    until StopCr( $g(t), m(t)$ )
     $c_i(t) \leftarrow R(t)$  [the  $i$ -th IMF] (Fig. 1(d))
     $s_{i+1}(t) \leftarrow s_i(t) - c_i(t)$ 
     $i \leftarrow i + 1$ 
end while
 $r(t) \leftarrow s_i(t)$  [the residual]
end procedure
function StopCr( $g(t), m(t)$ )
    if a stoppage criterion is satisfied then
        ▷ See Note 2 below.
        return true
    else
        return false
    end if
end function
  
```

Note 1: The decomposition completes when $s_i(t)$ becomes monotonic or has only one extremum.

Note 2: The sifting process stops if the IMF condition is satisfied. See also the text below.

In the algorithm of EMD/EEMD, some predetermined parameters such as ϵ , σ_e and N_e exist. The method of setting the parameters is discussed in [23]. The EMD/EEMD parameters used in this paper are shown in Table II.

B. Hilbert spectral analysis

The HHT can provide a time-frequency-energy paradigm of data. In this approach, the nonlinearity and nonstationarity can be extracted in a better manner than in the traditional paradigm of constant frequency and amplitude. For instance, the nonstationarity can be found directly from the IF and IA (see below). This is the reason that the Hilbert spectral analysis (HSA) was included as a part of the HHT.

The Hilbert transform of a function $u(t)$ is defined as

$$v(t) = \frac{1}{\pi} \text{P} \int_{-\infty}^{\infty} \frac{u(\tau)}{t - \tau} d\tau = u(t) * \left(\frac{1}{\pi t} \right), \quad (2)$$

where P and * denote taking the Cauchy principal value of the singular integral and the convolution, respectively. If a function $u(t)$ belongs to the Lebesgue space L^p for $1 < p < \infty$, the Hilbert transform is well defined and $g(t) = u(t) + iv(t)$ is the boundary value of a holomorphic function $g(z) = a(z)e^{i\theta(z)}$ in the upper half-plane [27,28]. Then, the instantaneous amplitude $A_{\text{inst}}(t)$ and the instantaneous phase function $\theta_{\text{inst}}(t)$ are defined by

$$A_{\text{inst}}(t) = \sqrt{u(t)^2 + v(t)^2}, \quad (3)$$

$$\theta_{\text{inst}}(t) = \tan^{-1} \left\{ \frac{v(t)}{u(t)} \right\}. \quad (4)$$

The instantaneous frequency $F_{\text{inst}}(t)$ is defined as

$$\begin{aligned} F_{\text{inst}}(t) &= \frac{1}{2\pi} \frac{d\theta_{\text{inst}}(t)}{dt} \\ &= \frac{1}{2\pi A_{\text{inst}}(t)^2} \left(u(t) \frac{dv(t)}{dt} - v(t) \frac{du(t)}{dt} \right). \end{aligned} \quad (5)$$

We emphasize that the meaning of the IF, which is a function of time, is very different from that of the Fourier frequency, which is constant by definition. Indeed, as the IF is a continuous function, it can reflect a modulation of a base frequency over a small fraction of the base wave cycle.

Through EMD/EEMD, we obtain the IMFs $c_i(t)$ (real part). From Eq. (2), we can obtain the imaginary part, or the conjugate function, of each $c_i(t)$. Therefore, the HSA derives $A_{\text{inst},i}(t)$ and $F_{\text{inst},i}(t)$ of each IMF $c_i(t)$. Through this procedure, the HHT allows us to extract instantaneous time-frequency and time-amplitude trajectories. This time-frequency-amplitude map (HHT map) allows for a high resolution time-frequency analysis of waveforms with strong frequency modulation.

III. SETUP FOR SIMULATION

In this section, we explain the setup for our data analysis simulation. We prepare the simulated time-series data of Advanced LIGO by combining Gaussian noise with a gravitational waveform from late inspiral, merger, and post-merger phases of BNS computed by numerical-relativity simulations.

A. Gravitational waveform from late inspiral, merger, and post-merger phases of BNS

We choose five GWs computed by Sekiguchi *et al.* [10,29]. These gravitational waveforms were computed for

NSs of two finite-temperature EOSs. One is a finite-temperature EOS which includes contributions of Λ hyperons (Hyp-EOS) [30], and the other is a purely nucleonic EOS (Shen-EOS). The maximum masses of zero-temperature spherical NSs for Hyp-EOS and Shen-EOS are $M_{\max, \text{Shen}} \approx 1.8M_{\odot}$ and $M_{\max, \text{Shen}} \approx 2.2M_{\odot}$, respectively. GWs were computed only for symmetric binaries with $M_{\text{NS}} = 1.35M_{\odot}$ and $1.5M_{\odot}$ for Hyp-EOS (referred to as H135 and H15) and Shen-EOS (S135 and S15), and $M_{\text{NS}} = 1.6M_{\odot}$ for Shen-EOS (S16). The characteristics of the models used in this paper are shown in Table I.

The waveforms consist of three parts: the late inspiral waveform, the merger waveform, and the post-merger waveform. Gravitational waves from the late inspiral phase are essentially identical to each other for the models with Hyp-EOS and Shen-EOS for the same mass. The waveforms in the merger and post-merger phases depend strongly on the total mass of binaries and the EOS. For all models used in this paper, a MNS is formed and the quasi-periodic GWs from the remnant MNS are emitted. Since the MNSs collapse to a black hole before relaxing to a stationary spheroid, the amplitude of quasi-periodic GWs damps steeply at the black hole formation for H135 and H15. The frequency of GW increases with time for H135 and H15 (Hyp-EOS models) [10], while it is approximately constant (around 2 kHz) for S135, S15 and S16 (Shen-EOS).

Detailed description of general relativistic numerical simulations and gravitational waveforms used in this paper are found in [10,29].

B. Simulation data

We use the simulated time-series noise data of Advanced LIGO. With a sensitivity curve of Advanced LIGO (the zero-detuned, high-power sensitivity curve [31]), we produce the simulated Gaussian noise in frequency domain. The sampling frequency f_{samp} is set to $f_{\text{samp}} = 1/\Delta t = 16384$ Hz, and the frequency range of the

TABLE I. Waveform models used in this paper. Maximum mass of Hyperon and Shen EOS are $1.8M_{\odot}$ and $2.2M_{\odot}$, respectively. Here, τ_{MNS} denotes the duration of the emission of quasi-periodic GWs from the MNS, and ρ_{opt} is the matched-filter signal-to-noise ratio of the post-merger signal evaluated for an optimally oriented source at 10 Mpc. Also, R_{opt} is the distance at which the post-merger signal produces $\rho_{\text{opt}} = 5$.

Model	$M_{\text{NS}}[M_{\odot}]$	$\tau_{\text{MNS}}[\text{ms}]$	ρ_{opt}	$R_{\text{opt}}[\text{Mpc}]$
H135	1.35	11	5.4	10.8
H15	1.5	3	4.1	8.2
S135	1.35	>25	5.6	11.2
S15	1.5	>25	6.2	12.4
S16	1.6	9	6.4	12.8

detector noise is set to be from 20 to 8182 Hz. Time-series noise data, $n(t)$, is produced by the inverse Fourier transform of the simulated noise in frequency domain.

The hypothetical observational data $s(t)$ is produced by injecting the GW signal $h(t)$ into the Gaussian noise $n(t)$; $s(t) = h(t) + n(t)$, where $h(t)$ can be expressed in terms of antenna pattern functions $F_{+}(\vec{e}_s(t))$ and $F_{\times}(\vec{e}_s(t))$, which depend on the direction of the source $\vec{e}_s(t) = (\theta_s(t), \phi_s(t))$, as well as polarizations components $h_{+}(t)$ and $h_{\times}(t)$ of the GWs as

$$h(t) = F_{+}(\vec{e}_s(t))h_{+}(t) + F_{\times}(\vec{e}_s(t))h_{\times}(t). \quad (6)$$

In this paper, since we consider optimally located sources at the zenith of a detector, we set $F_{+}(\vec{e}_s) = 1$ and $F_{\times}(\vec{e}_s) = 0$, for simplicity. We discuss the expected detectability of the post-merger signal with an optimal matched filter analysis. The strength of the signal is characterized by the matched-filter signal-to-noise ratio (SNR) ρ_{opt} defined as

$$\rho_{\text{opt}}^2 = 4 \int_{f_{\text{low}}}^{f_{\text{Nyq}}} \frac{|\tilde{h}(f)|^2}{S_n(f)} df, \quad (7)$$

where $\tilde{h}(f)$ is the Fourier transform of the signal, and $S_n(f)$ is the one-side power spectral density of noise. Here, f_{Nyq} and f_{low} are the Nyquist frequency and low frequency cutoff, respectively. If we set the threshold for the detection, ρ_{opt} , we obtain the maximum distance, R_{opt} , and the signal can be detected. Here, ρ_{opt} at 10 Mpc and R_{opt} for $\rho_{\text{opt}} = 5$ are listed in Table I.

Fig. 2 shows an example of data $s(t)$, where the H135 GW signal at a distance of 5 Mpc is injected into the simulated time-series noise data of Advanced LIGO.

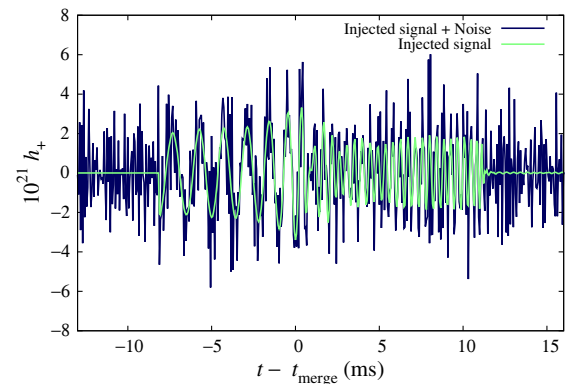


FIG. 2. Example of data $s(t)$. The black curve denotes signal $h(t)$ plus noise $n(t)$, and the green curve denotes the injected signal (H135) at 5 Mpc, where t_{merge} approximately denotes the time at which two stars come into contact.

IV. RESULTS OF HHT

In this section, we present the results of HHT analysis of the simulation data described in Sec. III.

A. IMF, IA, and IF

First, we apply the EEMD to each data set with the signal described in Sec. III B. For each of IMFs, we compute the IA and IF with HSA.

The values of EEMD parameters, which were discussed in Sec. II A 2, are summarized in Table II.

In Fig. 3, we show the results of HHT for the H135 GW signal at a hypothetical distance of 5 Mpc injected in Advanced LIGO noise. In this case, the data is decomposed into 8 IMFs, but those only from IMF1 to IMF6 are plotted, since it is clear that no GW signal is included in IMF7 and IMF8. The upper panel in each figure box shows $c_i(t)$ as the red curve and the injected signal as the dashed blue curve. The IA is plotted in the middle panel of each figure box, while the bottom panel shows the IF as the red curve, and the frequency of the injected signal as the dashed blue curve.

From this figure it is recognized that the IFs of IMF4 and IMF5, $F_{\text{inst},4}$ and $F_{\text{inst},5}$, clearly capture the frequency modulation in the late inspiral phase from -8 to 0 ms, even though the signal is split into two IMFs, and each IA, $A_{\text{inst},4}$ and $A_{\text{inst},5}$, is therefore smaller than the amplitude of the injected signal. The signal during this phase will be reconstructed more closely by adding the IMF4 and IMF5 together. Signals with a frequency band of 500 Hz or below would appear in IMF6 and higher IMFs if we used a longer-term waveform including earlier inspiral components. A significant decrease in $A_{\text{inst},4}$ is observed at $t = t_{\text{merge}}$, and thus, we may determine the merger time with reasonable accuracy. In any case, however, the matched filter method should attain higher accuracy than HHT for analysis of chirp signals in the inspiral phase.

IMF3 from 0 to 10 ms, on the other hand, captures the signal emitted from the MNS formed after the merger, while some portion of the signal is allotted to IMF2, especially in the later stage. The IF of IMF3, $F_{\text{inst},3}$, agrees substantially with that of the injected signal. However, $F_{\text{inst},3}$ stays in the same frequency band even after the black hole formation. During this period, IMF3 captures the noise

in that frequency band. As for the IA, $A_{\text{inst},3}$ decreases gradually even before the black hole formation. Therefore, it is difficult for the HHT to determine when the black hole is formed.

Based on the obtained IFs and IAs, we plot the time-frequency-amplitude map, which we call the HHT map, in the left of Fig. 4. In this figure, we use the time resolution $\Delta t = 1/16384$ s and frequency resolution $\Delta f = 20$ Hz. The frequency evolution can be seen clearly, and it agrees approximately with that of the injected signal.

We show the HHT map and its enlargement for S15 in the right of Fig. 4. We also plot the $F_{\text{inst},3}$ in the post-merger phase for H135 and S15 as functions of time in Fig. 5.

As already pointed out in [10] and discussed in Sec. III A, the frequency of GWs from MNS increases with time for Hyp-EOS, while the frequency is approximately constant (besides a periodic oscillation) for Shen-EOS. Figure 5 indeed shows that the IF of H135 increases overall until 10 ms, while the IFs of S15 is essentially constant until 12 ms, when a black hole is formed. We may therefore distinguish the difference of the frequency evolution between Hyp-EOS models and Shen-EOS models.

B. Statistical error

Since we generate the detector noise $n(t)$ with a Gaussian random variate, the results of the analysis will be changed even for the same injected signal if a different seed of random numbers is used. Since the (E)EMD is a data-driven decomposition method, the results of the HHT may be affected by the different realization of noise. Therefore, we investigate the statistical property of the results of the HHT. We perform the HHT for 1000 samples, each of which is generated by adding a Gaussian random variate with a different seed.

The result for the H135 signal at a hypothetical distance of 5 Mpc is shown in Fig. 6. Each of the top panels shows the mean value of the IA for corresponding IMF as the red curve and its standard deviation ($\pm 1\sigma$) as the green shaded region. In each of the bottom panels, we plot the mean value of the IF (red curve) for corresponding IMF and its standard deviation ($\pm 1\sigma$) (green shaded region) as well as the frequency of the injected signal (dashed blue curve), which is computed from $h_+(t)$ and $h_\times(t)$ obtained by numerical-relativity simulations.

We find that the standard deviation of the IF is smaller in the period when the IA of the corresponding IMF is larger. We also find that the $F_{\text{inst},3}$ from 0 to 10 ms agrees with the frequency of GWs emitted after the merger very well. Similarly, the $F_{\text{inst},4}$ from -10 to 0 ms agrees with the frequency of GWs emitted in the late inspiral and the IF of $F_{\text{inst},5}$ from -10 to -5 ms agrees with the frequency of the first half of the late inspiral. On the other hand, the standard deviation of the IF of each IMF are large when there exists only noise.

TABLE II. EEMD parameters.

Model	ϵ	σ_ϵ	N_ϵ
H135	10^{-6}	0.5	200
H15	10^{-4}	0.5	200
S135	10^{-4}	0.5	200
S15	10^{-6}	0.5	200
S16	10^{-2}	1.0	200

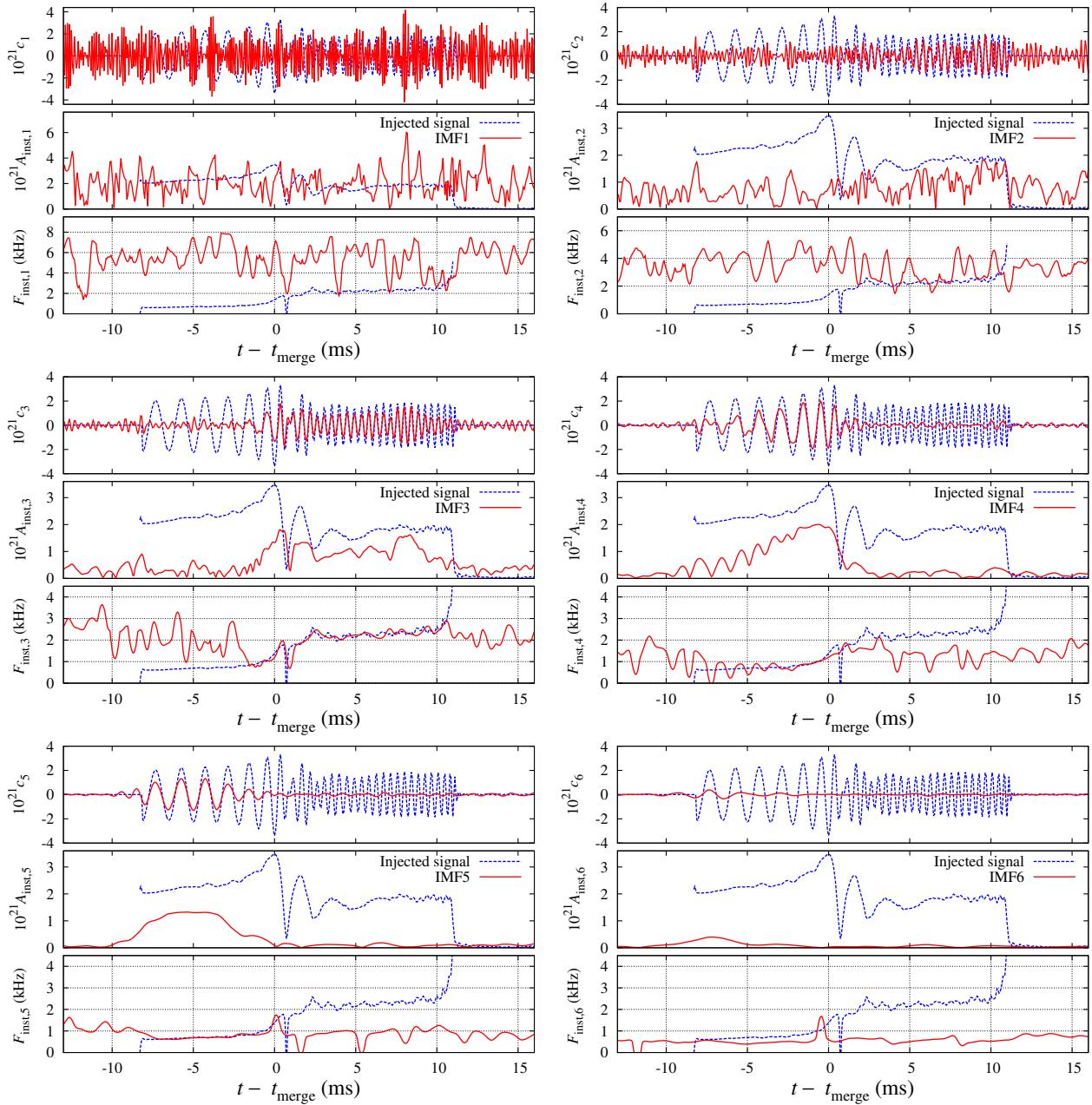


FIG. 3. A result of HHT. GW signal H135 at a hypothetical distance of 5 Mpc injected in Advanced LIGO noise is used. The upper panel in each figure box shows the IMF $c_i(t)$ (red curve) as well as the injected H135 waveform (dashed blue curve). The middle panel shows the IA of corresponding IMF. The bottom panel shows the IF of the corresponding IMF (red curve) as well as the frequency of injected signal (dashed blue curve).

For other injected signals given in Table I, we generally obtained the similar results to those discussed in Secs. IV A and IV B.

C. Characteristics of frequency evolution

From the discussion in Sec. IV A, we may distinguish the difference of the frequency evolution between Hyp-EOS models and Shen-EOS models. In this subsection, we characterize the frequency evolution by using the linear regression.

We make the linear regression for $F_{\text{inst},3}$ using the least squares method with weights:

$$F_{\text{inst},3}(t) = \beta_1 + \beta_2 t, \quad (8)$$

with the fitting time range from 3 to 11 ms for H135 and from 3 to 12 ms for S15. The coefficient of β_1 and β_2 are the intercept and gradient, respectively. The frequency evolutions are characterized with the gradient β_2 .

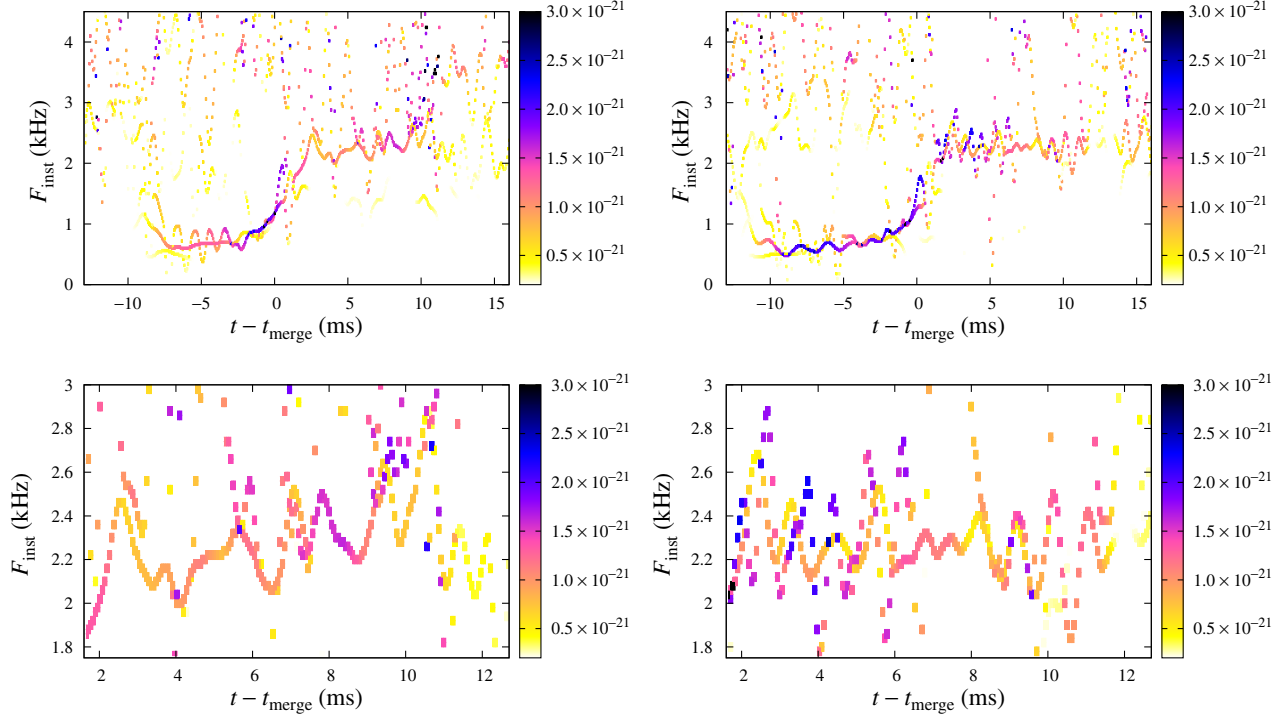


FIG. 4. Time-frequency-amplitude map (HHT map). The color bar denotes the value of the IA. The GW signal H135 (left top) and S15 (right top) at a hypothetical distance of 5 Mpc are used. The left and right bottom figures are the enlargement of left and right top figures, respectively.

Using the results in Sec. IV B, we perform the fitting to evaluate the coefficient β_2 from 1000 samples. Figure 7 shows the distribution of β_2 for H135 (purple region) and S15 (green region). The mean and the standard deviation of β_2 become (40.3 ± 18.7) Hz/ms for H135 and (5.4 ± 12.2) Hz/ms for S15. From these results, we can confirm that $F_{\text{inst},3}$ increases with time for H135, while $F_{\text{inst},3}$ is approximately constant for S15. This fact suggests the possibility that we can distinguish the EOS from the evolution of the IF of MNS by using the HHT analysis. Note, however, that since the distribution of β_2 for H135 and S15 overlap each other in Fig. 7, there is a possibility

that we cannot distinguish the frequency evolution clearly at this distance.

V. ACCURACY OF THE FREQUENCY EVOLUTION

Now we focus on the GWs emitted in the merger and post-merger phases. A MNS is formed after the merger for the models considered in this paper. We now examine how accurately we can measure the GW frequency from MNS with the HHT.

In order to evaluate the measurement accuracy of the IF of GWs from MNS, we define [23]

$$\delta = 100 \times \frac{\text{WTSS}[F_{\text{inst},i}(t) - F_{\text{signal}}(t)]}{\text{WTSS}[F_{\text{signal}}(t)]}, \quad (9)$$

$$\text{WTSS}[F_{\text{inst}}(t)] = \sum_j A_{\text{inst}}^2(t_j) F_{\text{inst}}^2(t_j), \quad (10)$$

where $F_{\text{signal}}(t)$ is the frequency of the injected signal.

We evaluate δ by using the IF and IA of IMF c_2 or c_3 for each model listed in Table I. In Table III, we show the mean value of δ and the standard deviation for an event at a distance of 10 Mpc. The mean values and the standard deviation of δ are plotted as functions of the source distance in Fig. 8.

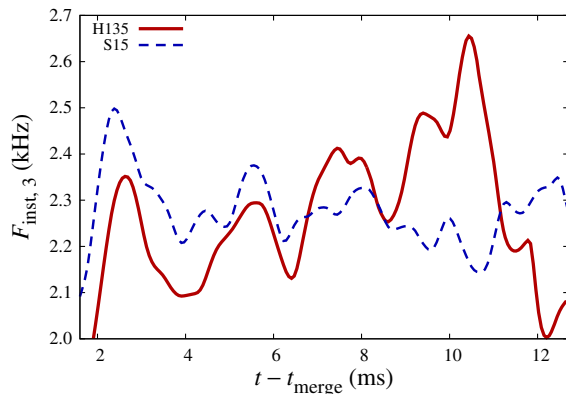


FIG. 5. The $F_{\text{inst},3}$ for H135 (solid red curve) and S15 (dashed blue curve), as functions of time in post-merger phase.

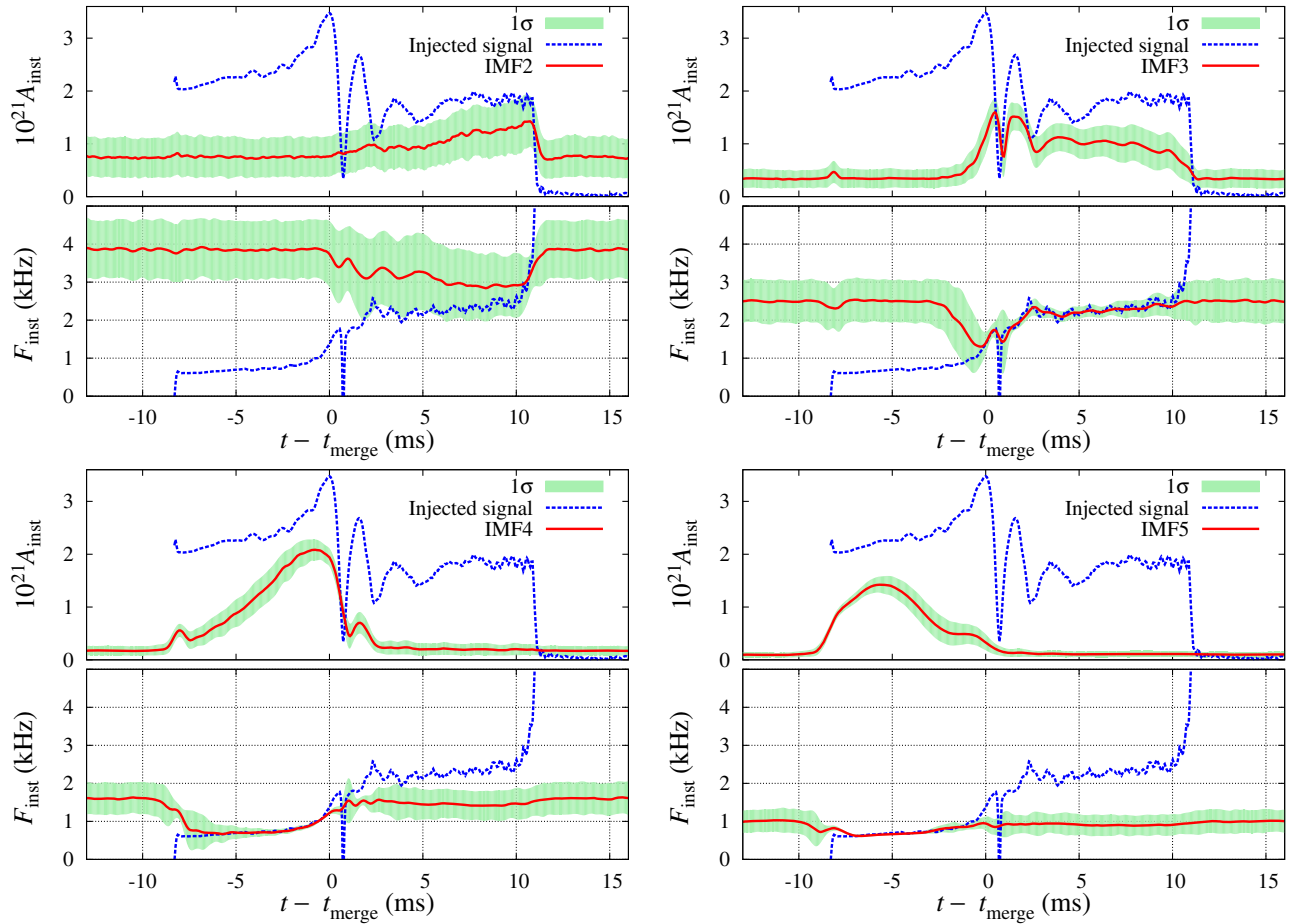


FIG. 6. Example of statistical property of the IA and IF. The GW signal H135 at a hypothetical distance of 5 Mpc is used. Each upper panel shows the mean of IA (red curve) of corresponding IMF and its standard deviation ($\pm 1\sigma$) (green shaded region). Each bottom panel shows the mean IF of the corresponding IMF (red curve) and its standard deviation ($\pm 1\sigma$) (green shaded region) as well as the frequency of the injected signal (dashed blue curve).

We find that if the time duration of quasi-periodic GWs emitted from the MNS is long enough, the frequency modulation can be evaluated with good accuracy for Hyp-EOS and Shen-EOS cases. For example, although for H15, δ is about 30% at 10 Mpc, δ is less than 5% for other models. This difference can be explained from the duration of the quasi-periodic GWs emitted from MNS in Table I.

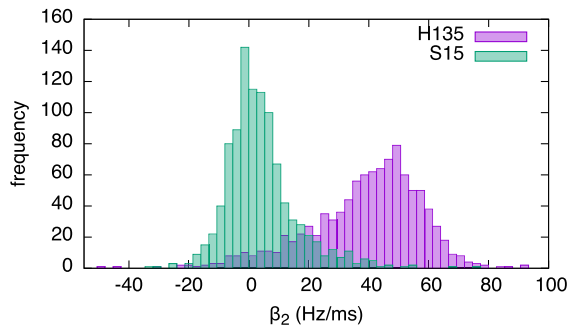


FIG. 7. Distribution of β_2 for H135 (purple region) and S15 (green region).

In the previous study [13], the relation between the peak frequency of the Fourier spectrum f_{peak} and the radius parameter $R_{1.8}$, which is the radius of a cold, spherical neutron star of mass $1.8M_{\odot}$ in general relativistic hydrostatic equilibrium, was discussed. It is given as

$$f_{\text{peak}} = (4.0 \pm 0.3) \text{ kHz} \left(\frac{(R_{1.8}/\text{km}) - 2}{8} \right)^{-3/2}. \quad (11)$$

TABLE III. The value of $\delta \pm 1\sigma$ for an event at a hypothetical distance of 10 Mpc. Range (the third column) denotes the time duration of summation in Eq. (10).

Model	IMF	Range [ms]	$\delta \pm 1\sigma$ [%]
H135	3	[2, 11]	2.4 ± 1.2
H15	3	[2, 3]	29.6 ± 8.5
S135	3	[2, 12]	3.0 ± 3.6
S15	3	[2, 12]	1.0 ± 0.6
S16	2	[2, 9]	2.0 ± 0.8

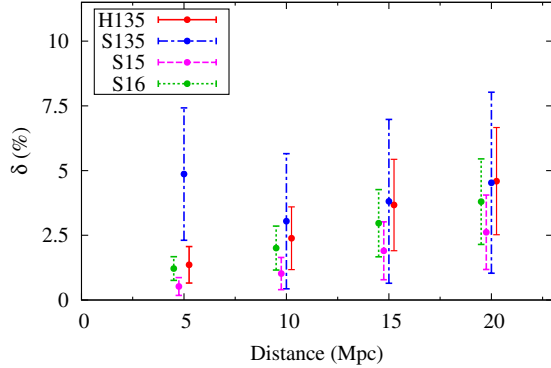


FIG. 8. The value of δ as a function of the source distance. The marks mean the value of δ for 1000 realizations, and the error bars are its standard deviation.

The peak frequency f_{peak} can be evaluated from the time integration of the IF. For models other than H15, since δ is the square-sum of difference between the IF of IMF and the injected signal, the measurement error of f_{peak} may be much smaller than the value of δ . By using the $f_{\text{peak}} - R_{1.8}$ relation given by Eq. (11), the measurement accuracy of the IF is transformed into the accuracy of $R_{1.8}$ within a few hundred meters.

VI. SUMMARY

We performed the HHT analysis of GWs emitted from the late inspiral, merger, and post-merger phases of coalescence of BNSs. We used the waveforms computed by general relativistic numerical simulations and the simulated time-series noise data of Advanced LIGO. From the results of the HHT analysis, we found that the frequency evolution can be seen clearly on the time-frequency map, and that the frequency evolution agrees with that of the injected signals. As pointed out in [10] and discussed in Sec. III A, the frequency of GWs from MNS increases with time for Hyp-EOS, while the frequency is overall unchanged for Shen-EOS. We confirmed that we can distinguish the difference of the frequency evolution between Hyp-EOS models and Shen-EOS models in Secs. IV A and IV C. This fact suggests a possibility that we may be able to distinguish the EOS from the evolution of the IF of MNS by using the HHT analysis.

We also investigated the statistical property of the measurement accuracy of the IF for each of injected signals. We found that for models in which MNS signals last for 10 ms or more, the frequency modulation can be evaluated

with error less than 5% for an event at a distance of 10 Mpc. These results suggest that we can evaluate the radius parameter $R_{1.8}$ with accuracy within a few hundred meters if a nearby (lucky) event is detected by Advanced LIGO.

The peak frequency can also be evaluated by using usual Fourier spectrum of data. In that sense, the peak frequency derived from the HHT is just an additional evidence of the peak frequency. Note, however, that, as stated above, the information which can be obtained by the HHT analysis is not limited to the peak frequency. We can also clearly observe the frequency evolution of the signals. This is one of the most important advantages of the HHT analysis.

In this paper, we assumed that the sources are located at the distance of 5 or 10 Mpc. The expected detection rate at 10 Mpc is $\sim 10^{-4} - 0.1$ events yr^{-1} [5]. Thus, Advanced LIGO, Advanced Virgo and KAGRA may not observe BNS coalescences at such distance. On the other hand, in the case of a planned future detector, such as the Einstein Telescope [32], the detectable distance will be increased by factor of ~ 10 . In that case, the expected event rate becomes $\sim 0.1 - 100$ events yr^{-1} . Thus, we may have to wait until such future detectors are realized before the HHT analysis of MNS signals presented in this paper become useful.

In this paper, we used simulated Gaussian noise of Advanced LIGO. However, the noise of real laser interferometer detectors show non-Gaussianity and nonstationarity. Therefore, we are planning to apply our method to real laser interferometer data in the near future.

ACKNOWLEDGMENTS

The authors would like to thank Jordan B. Camp for many discussions about topics related to the research presented here. This work was in part supported by MEXT Grant-in-Aid for Scientific Research on Innovative Areas “New Developments in Astrophysics Through Multi-Messenger Observations of Gravitational Wave Sources” (Grant No. 24103005). This work was also supported in part by JSPS Grant-in-Aid for Young Scientists (B) (Grant No. 26800129; H. Takahashi.), by JSPS Grant-in-Aid for Scientific Research (C) (Grant No. 15K05071; K.O., Grants No. 23540309 and No. 15K05081; H. Tagoshi), and JSPS Grant-in-Aid for Scientific Research (A) (Grant No. 24244028; M. S., Y. S., and H. Tagoshi), and JSPS Grant-in-Aid for Scientific Research (A) (Grant No. 16H02183; M. S.).

- [1] J. Abadie *et al.*, *Classical Quantum Gravity* **32**, 074001 (2015).
- [2] B. P. Abbott *et al.*, *Phys. Rev. Lett.* **116**, 061102 (2016).
- [3] T. Acernese *et al.*, *Classical Quantum Gravity* **32**, 024001 (2015).
- [4] K. Kuroda, *Classical Quantum Gravity* **27**, 084004 (2010).
- [5] J. Abadie *et al.*, *Classical Quantum Gravity* **27**, 173001 (2010).
- [6] J. M. Lattimer and M. Prakash, *Phys. Rep.* **442**, 109 (2007).
- [7] P. Demorest, T. Pennucci, S. Ransom, M. Roberts, and J. Hessels, *Nature (London)* **467**, 1081 (2010).
- [8] J. Antoniadis *et al.*, *Science* **340**, 1233232 (2013).
- [9] K. Hotokezaka, K. Kyutoku, H. Okawa, M. Shibata, and K. Kiuchi, *Phys. Rev. D* **83**, 124008 (2011).
- [10] Y. Sekiguchi, K. Kiuchi, K. Kyutoku, and M. Shibata, *Phys. Rev. Lett.* **107**, 211101 (2011).
- [11] A. Bauswein and H.-T. Janka, *Phys. Rev. Lett.* **108**, 011101 (2012).
- [12] A. Bauswein, H.-T. Janka, K. Hebeler, and A. Schwenk, *Phys. Rev. D* **86**, 063001 (2012).
- [13] K. Hotokezaka, K. Kiuchi, K. Kyutoku, T. Muranushi, Y. Sekiguchi, M. Shibata, and K. Taniguchi, *Phys. Rev. D* **88**, 044026 (2013).
- [14] K. Takami, L. Rezzolla, and L. Baiotti, *Phys. Rev. Lett.* **113**, 091104 (2014).
- [15] J. Clark, A. Bauswein, L. Cadonati, H.-T. Janka, C. Pankow, and N. Stergioulas, *Phys. Rev. D* **90**, 062004 (2014).
- [16] J. Clark, A. Bauswein, N. Stergioulas, and D. Shoemaker, *Classical Quantum Gravity* **33**, 085003 (2016).
- [17] N. Huang, S. Long, and Z. Shen, *Adv. Appl. Mech.* **32**, 59 (1996).
- [18] N. Huang, Z. Shen, S. Long, M. Wu, H. Shih, Q. Zheng, N. Yen, C. Tung, and H. Liu, *Proc. R. Soc. A* **454**, 903 (1998).
- [19] N. Huang, Z. Shen, and S. Long, *Annu. Rev. Fluid Mech.* **31**, 417 (1999).
- [20] J. B. Camp, J. K. Cannizzo, and K. Numata, *Phys. Rev. D* **75**, 061101 (2007).
- [21] A. Stroeer, J. K. Cannizzo, J. B. Camp, and N. Gagarin, *Phys. Rev. D* **79**, 124022 (2009).
- [22] A. Stroeer, L. Blackburn, and J. B. Camp, *Classical Quantum Gravity* **28**, 155001 (2011).
- [23] H. Takahashi, K. Oohara, M. Kaneyama, Y. Hiranuma, and J. B. Camp, *Adv. Adapt. Data Anal.* **05**, 1350010 (2013).
- [24] M. Kaneyama, K. Oohara, H. Takahashi, Y. Hiranuma, T. Wakamatsu, and J. B. Camp, *ICIC Express Lett., Part B: Appl.* **5**, 285 (2014).
- [25] M. Kaneyama, K. Oohara, Y. Sasaki, H. Takahashi, and J. B. Camp, *ICIC Express Lett., Part B: Appl.* **6**, 343 (2015).
- [26] Z. Wu and N. Huang, *Adv. Adapt. Data Anal.* **01**, 1 (2009).
- [27] L. Cohen, *Time Frequency Analysis: Theory and Applications*, (Prentice Hall, New York, 1995).
- [28] B. V. Khvedelidze, *Encyclopaedia of Mathematics* (Springer, New York, 1989).
- [29] Y. Sekiguchi, K. Kiuchi, K. Kyutoku, and M. Shibata, *Phys. Rev. Lett.* **107**, 051102 (2011).
- [30] H. Shen, H. Toki, K. Oyamatsu, and K. Sumiyoshi, *Astrophys. J. Suppl. Ser.* **197**, 20 (2011).
- [31] <https://dcc.ligo.org/cgi-bin/DocDB/ShowDocument?docid=2974>.
- [32] S. Hild *et al.*, *Classical Quantum Gravity* **28**, 094013 (2011).